Functional Acrylate Resins for Shape Memory Polymer Microarchitectures

Erika Salzman

Senior Bachelor's Thesis
Materials Science
California Institute of Technology
Spring 2020

Principal Investigator: Julia Greer

Table of Contents

I. Abstract

Shape memory polymers (SMPs) are materials that can undergo programmable shape change in response to a specific stimulus. The ability to undergo this reliable, three-dimensional shape change makes SMPs promising smart materials for applications like biomedical stents and sutures. However, to access areas like blood vessels in the eye, these materials must be fabricated with micron or submicron resolution. In this work, benzyl methacrylate-based, heat-responsive SMP microstructures were fabricated using two-photon lithography in a variety of three-dimensional designs. The effects of different fabrication conditions on the structures were studied, and Raman spectroscopy was used to probe network properties, including degree of polymerization.

The resin was also chemically functionalized prior to polymerization with BOC-protected amine groups via the thiol-Michael addition reaction, which allows for attachment of other useful functional groups to the surface of the structures. This chemistry was utilized for attachment of a dye as well as gold nanoparticles. When exposed to laser light, these nanoparticles can undergo localized surface plasmon resonance and serve as heat generators. The theoretical feasibility of using this heating technique to induce shape change in SMP microstructures is examined in this work.

II. Introduction

Shape memory polymers (SMPs) are highly elastic materials that are able to store "memory" of their original (permanent) shape and reassume this shape after being deformed into a different (temporary) shape in response to a specific thermal, electrical, or other stimulus. Temperature-sensitive SMPs are comprised of a set of crosslinking net points that are connected by a network of long chains. Heating these materials above a certain critical temperature (often the glass transition or melting temperature) introduces energy into the network, increasing the mobility of the chains and allowing them to be stretched or compressed under external stress, thereby changing the overall shape of the polymer. Subsequently cooling the polymer below its critical temperature while maintaining external stress freezes the network in an entropically unfavorable, temporary shape. The temporary network state will remain stable due to lack of movement in the chains until the polymer is heated above its critical temperature, which grants the chains energy and mobility. The network will then return to its most entropically favorable configuration associated with the permanent shape (Figure 1).[1,2]

SMPs have shown promise for use in biomedical applications such as vascular stents, minimally invasive sensors, drug delivery systems, tissue scaffolds, and artificial skin.[3,4] SMPs are an attractive alternative to shape memory alloys in many of these applications due to their low cost, tailorable transition temperatures, and potential for biocompatibility.[2] Incorporating functional groups into these SMPs introduces further applications for these materials in which control over chemical functionality is necessary. SMPs can be fashioned into nearly any shape desired via methods like 3D printing[5] and into simple microscale structures via traditional lithography

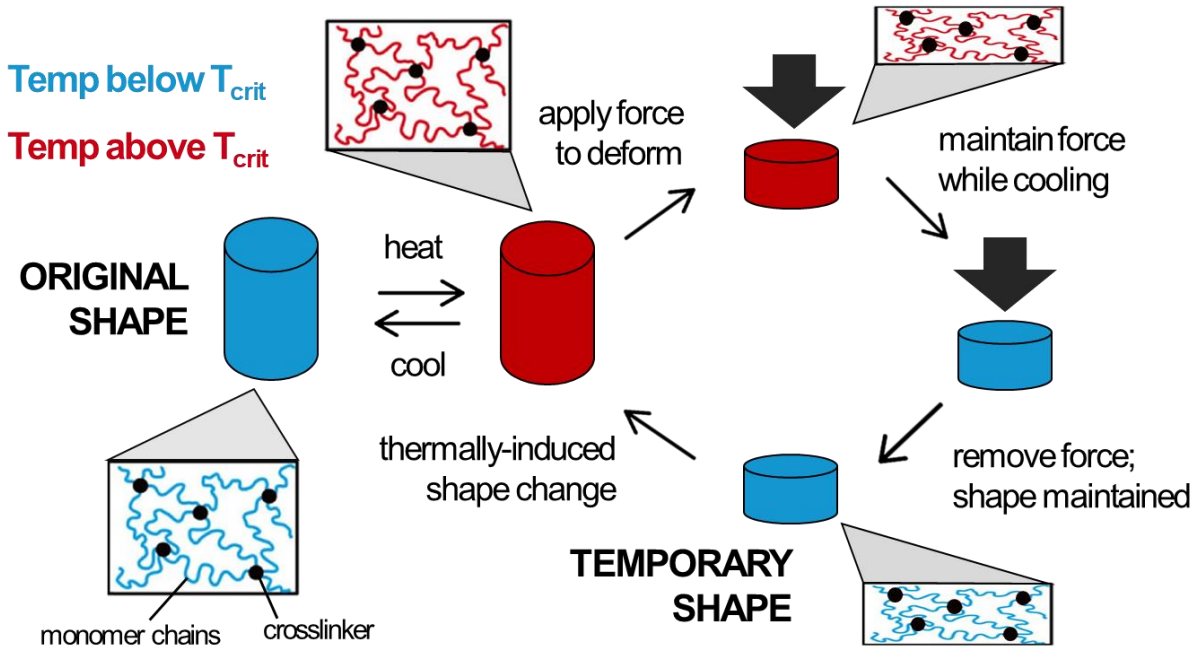

Figure 1. A typical shape memory cycle. The repeatable cycle of heating, applying force, and cooling is accompanied by stretching and relaxation of chain segments (colored lines) and shifts in the relative location of crosslinking net points (black dots). Adapted from Zhao et al.[1]

techniques. However, these two aspects – tailored design and micron length scales – must be combined to utilize SMPs in areas of limited space like blood vessels in the eye.

To allow for both these qualities, a technique called two-photon lithography (TPL) can be utilized. TPL is a fabrication technique for creating three-dimensional architectures of almost any conceivable design in a wide variety of compositions with sub-micron definition. In TPL of polymer materials, a liquid resin called a photoresist containing photoinitiator and polymer components is exposed to a focused beam of laser light in the infrared. Absorption of a single low-energy photon of this wavelength does not provide enough energy to initiate photopolymerization, allowing the beam to penetrate through the resin. However, at the focal point of the beam, the probability of two photons being absorbed simultaneously increases significantly, which initiates radical polymerization reactions and solidifies that photoresist in that area. The reactions propagate

in a very small region (80-800 nm in the plane perpendicular to beam propagation and 3 to 5 times further in the direction of beam propagation) dictated by the position of the focal point. The focal point can be moved throughout the volume of the photoresist, allowing for the fabrication of complex 3D structures without the need for external supports.[6,7]

Recently, Yee et al. developed a TPL-compatible, functional photoresist comprised of an acrylate crosslinker with tert-butyloxycarbonyl (BOC)-protected amine groups added before TPL via the thiol-Michael addition reaction.[8] In this work, Yee's method was used to create components for a new polymer resin including amine functionalized 3-(acryloyloxy)-2-hydroxypropyl methacrylate (FMA) and poly-benzyl methacrylate (pBMA) as monomers and amine functionalized pentaerythritol triacrylate (PETA) as a crosslinker (Figure 2). When cured under UV light, macroscale samples of this resin have shown shape memory recovery behavior at temperatures as low as 40 °C, which is likely the result of the inclusion of long chains in the resin,

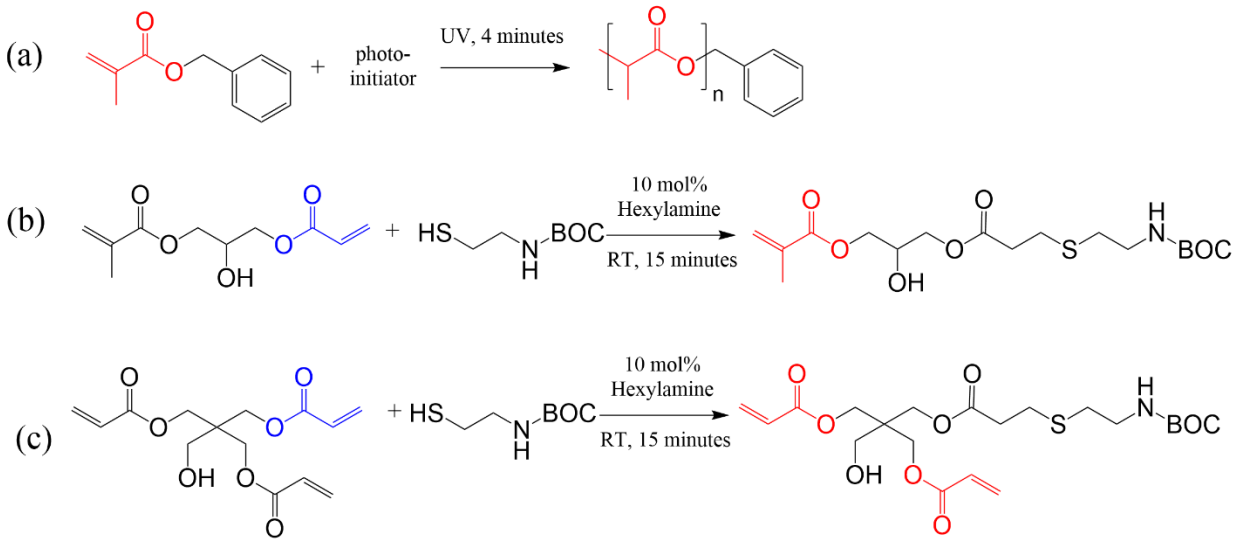

Figure 2. Reaction schemes for network components: (a) BMA and pBMA, (b) functionalized methacrylate, (c) and functionalized PETA. Acrylate groups highlighted in blue undergo functionalization, and the acrylate and methacrylate groups highlighted in red are unreacted and available for network formation post-functionalization.

particularly pBMA. Transition temperatures near human body temperature (~37 °C) are ideal for use within the body and for storage at room or refrigerator temperature.

After iterating through multiple resin compositions, including some with a different crosslinker, a PETA-containing resin has been successfully adjusted for compatibility with TPL and has been used to print a variety of microarchitectures including thin plates, cylindrical pillars, lattices, and other more complicated structures. The networks in these structures were characterized via Raman spectroscopy, and estimates of their degrees of polymerization were made. Finally, the possibility of utilizing the amine functionality of the structures to attach gold nanoparticles was explored. Gold nanoparticles are known to generate heat via localized surface plasmon resonance, and the possibility of using this method to induce shape change in the SMP microstructures was explored from a theoretical perspective.

III. Results & Discussion

A. Resin Screening Process

Rapid Bending Test

To identify compositions with promising shape memory properties for later fabrication of architectures by TPL, a standardized bending test adapted from Li et al.[9] was developed to measure three shape memory characteristics of different resin compositions. These characteristics included deformability (D), the maximum deformation that the material can tolerate; fixed deformation (FD), the ability of the material to retain deformed shape over time; and shape recovery (SR), the ability of the material to recover their original shapes after reheating to various temperatures.

To perform the bending test, equal aliquots of each resin tested were poured into u-shaped polydimethylsiloxane (PDMS) molds (Figure 3b) made from a 3D printed polylactic acid (PLA) mold box (Figure 3a) prior to resin polymerization, ensuring that the samples had consistent shapes and dimensions. After polymerization but before heating or deformation, samples were marked on their surfaces with three dots in the approximate locations shown in Figure 3d to enable consistent measurement of the angle formed by each polymer sample.

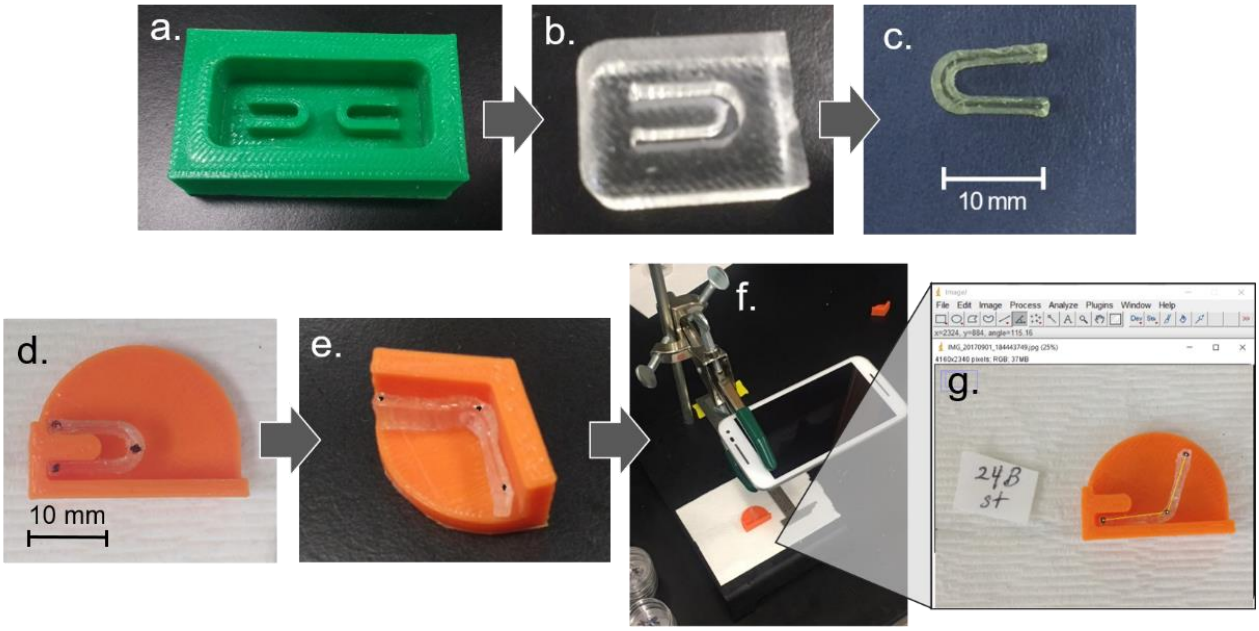

Figure 3. Bending test procedure. (a) PLA mold boxes were used to make (b) PDMS molds for (c) u-shaped polymer samples. The samples were then (d) marked with three black dots for consistent angle measurement. Samples were heated above T_g and (e) deformed to the angle of the guide. (f) The setup shown was used to take (g) pictures of the samples for digital analysis.

Bending Test Results for Pentaacrylate Resin

The bending test described was performed on a series of resin compositions containing varying mole percents of chain builders – benzyl methacrylate (BMA) and functionalized 3-(acryloyloxy)-2-hydroxypropyl methacrylate (FMA) – and functionalized dipentaerythritol pentaacrylate (DPEPA), a crosslinker similar to pentaerythritol triacrylate containing more

acrylate groups for polymer branching (Table 1). Benzyl methacrylate was chosen for its high failure strength and strain compared to other similar acrylates and methacrylates.[10] 3-(acryloyloxy)-2-hydroxypropyl methacrylate was chosen for functionalization due to its asymmetric structure; acrylate groups have been shown to be more reactive in Michael additions than methacrylate groups, allowing for better prediction of product distribution of the chain builder after functionalization.[11] Ultimately, PETA was used instead of DPEPA due to DPEPA's higher T_g, high viscosity, and difficulties adapting the resin for TPL. However, the bending test results using DPEPA still show valuable trends in shape memory characteristics for different compositions.

Table 1. Compositions of resins for bending test.

ID	*DPEPA mol%*	*BMA mol%*	*FMA mol%*	*Molar ratio BMA:FMA*
D1.0BF8	1.0	86.9	10.9	8:1
D2.5BF8	2.5	84.0	10.5	8:1
D4.0BF8	4.0	81.0	10.1	8:1
D5.5BF8	5.5	78.0	9.8	8:1
D1.0BF16	1.0	92.0	5.8	16:1
D2.5BF16	2.5	88.9	5.6	16:1
D4.0BF16	4.0	85.8	5.4	16:1

To measure fixed deformation (FD), the u-shaped samples were heated to 80 °C (≥ 20 °C above the onset temperature of deformation for all samples) and bent open to a consistent angle of approximately 110° using a 3D printed PLA angle guide (Figure 3e). While maximum deformability measurements were not taken for this study, this step served as a screening technique, ensuring that samples had deformability values of at least 110° in this experimental setup. Samples were held in the shape of the guide and submerged in a water bath for 10 seconds, allowing them

to cool to room temperature while under external force. Samples were stored at room temperature, and pictures of the samples were taken over time until 7 days after angles were set. With the aid of the three marks made the samples' surfaces, the angles of the samples were measured digitally using the software ImageJ. These angle data (Figure 4a) were used to calculate the average FD value for each composition using the formula:

$$FD = \frac{\theta_{\text{fixed}}}{\theta_{\text{max}}} \cdot 100\% \qquad (1)$$

where θ_{max} is defined as the angle immediately after programming and θ_{fixed} is defined as the angle after a given amount of time. Results of these calculations are shown in Figure 4 and Table S1.

All samples showed a decrease in angle over time, but the most substantial change in most samples' angles occurred between day 0 and day 3. At lower crosslinker concentrations (compositions D1.0BF8, D2.5BF8, D1.0BF16, D2.5BF16), samples maintained their angles quite

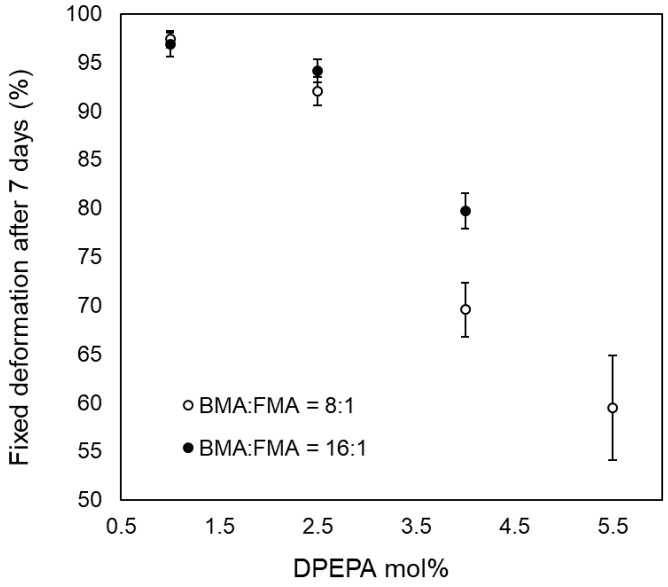

Figure 4. Fixed deformation data. Mean FD values measured for different compositions (n=5 for each composition) after 7 days at room temperature. An FD value of 100% indicates the sample completely maintains the initial deformation, while and FD value of 0% indicates the sample returned completely to its original shape.

well, with FD values between 90% and 98%, but these compositions appeared to have similar FD behavior to one another, including with different BMA:FMA ratios. The remaining three compositions (D4.0BF8, D5.5BF8, and D4.0BF16) all had significantly less ability to hold their deformed shapes (lower FD values). At these higher crosslinker concentrations, it appears possible that increasing BMA:FMA may increase FD values, but this is cannot be concluded without testing a sample with 5.5 mol% DPEPA and a BMA:FMA ratio of 16:1. Overall, a crosslinker concentration of at most 2.5 mol% is necessary to provide high FD at room temperature.

To measure shape recovery (SR), pictures of the unheated, undeformed u-shaped samples were taken to establish their minimum achievable angle associated with the permanent shape. The samples were then heated to 80 °C and bent open to a consistent angle (~110°) using the PLA angle guide as used for FD measurement and cooled to room temperature in a water bath while being held in the open position. Pictures were taken of the samples and their angles measured digitally to establish the maximum angle to which each sample was opened. The samples were then placed on a hot plate, heated to various temperatures, and held at those temperatures for 15 minutes. The samples were removed from the hot plate and had their angles measured as before. This procedure was performed at 40 °C, 55 °C, and 70 °C in succession. These angle data were used to calculate the average SR for each composition at each temperature using the formula:

$$\mathrm{SR} = \frac{\theta_{\max} - \theta_{\mathrm{heated}}}{\theta_{\max} - \theta_{\min}} \cdot 100\% \qquad (2)$$

where $\theta_{\max}$ was defined as the angle immediately after programming, θ_{heated} was defined as the angle after heating at a given temperature for 15 minutes, and $\theta_{\min}$ was defined as the angle prior to any deformation. Results of these calculations are shown in Figure 5 and Table S1.

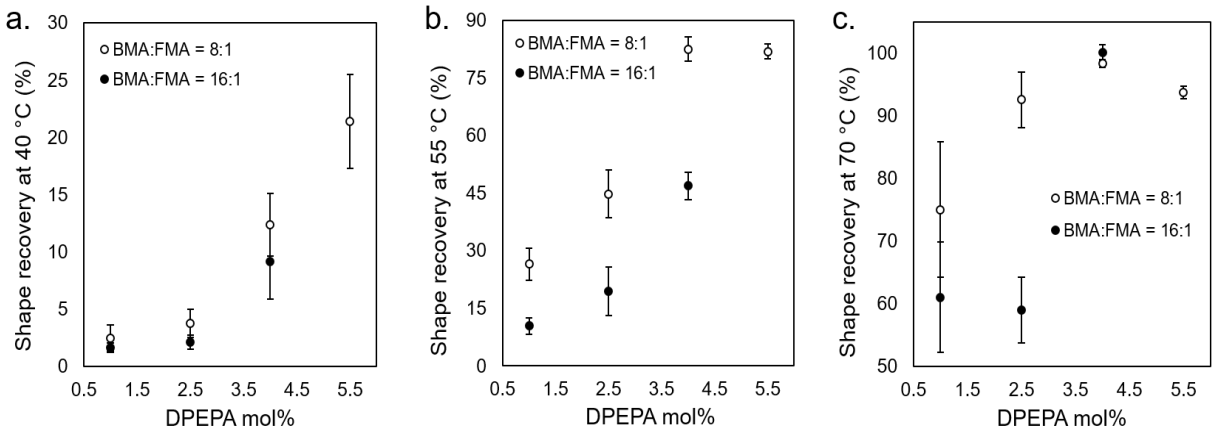

Figure 5. Shape recovery data. Mean SR values calculated for different compositions (n=5 for each composition) after being held at (a) 40 °C, (b) 55 °C, and (c) 70 °C. An SR value of 100% indicates the sample completely recovered its original shape, while an SR value of 0% indicates the sample did not recover any amount towards its original shape.

All the compositions showed an increase in SR as the temperature at which they were held increased, and at 70 °C, samples of composition D2.5BF8 and D5.5BF8 had recovered substantially toward their original shapes (90% < SR < 95%) after 15 minutes, and compositions D4.0BF8 and D4.0BF8 had nearly completely recovered their original shapes (SR > 98%). Additionally, at 55 °C, compositions D4.0BF8 and D5.5BF8 had recovered their original shapes a substantial amount (80% < SR < 85%). These results indicate that a DPEPA concentration of 4 mol% or more gives the best SR results in the tested temperature range, although there does not appear to be a clear difference between 4 mol% and 5.5 mol% DPEPA.

Overall, these bending tests have shown that, in the ranges tested, increasing crosslinker concentration tends to correspond to increasing ability to recover shape after heating (high SR) but a decreasing ability to maintain mechanical deformation at room temperature (low FD). This trade-off is likely correlated to the roll that crosslinking net points play in SMPs on the molecular level; the driving force for SMPs to return to their permanent shape comes from the tendency toward the

lowest energy state, which occurs when the net points have returned to their original relative positions. A higher crosslinker concentration also implies that the average chain length in the polymer network is shorter, meaning that the number of entropic states for the network at a given temperature is smaller, which increases the probability that the network will return to its original arrangement.

Samples with higher crosslinker concentrations were consistently able to recover closer to their permanent shapes at lower temperatures than those with lower crosslinker amounts, suggesting that compositions containing more crosslinker would be the most useful for lower temperature applications, including the biomedical applications mentioned. However, these compositions are less able to fix deformation at room temperature. Storing these compositions at lower ambient temperatures, in a refrigerator for example, may sufficiently decrease the thermal energy in the network to allow the samples with higher crosslinker concentrations to have increased FD values.

The data also seem to suggest that higher BMA:FMA ratios appear to grant better fixed deformation, but worse shape recovery. These facts are consistent with the hypothesis that benzene ring interactions may stabilize the confirmation of the network, allowing compositions to hold their shape more effectively but also causing them to require more energy to overcome these interactions to return to their original shape. These effects are not consistent across all compositions tested, however, and further testing would be required to make such a conclusion.

Some microstructures of the DPEPA-containing photoresist (composition D4.0BF8) were fabricated by two-photon lithography (Figure S1). However, this photoresist required very slow scan speeds to fully polymerize and did not produce ideal structures. Eventually a new resin

composition was formulated using a different crosslinker, pentaerythritol triacrylate, and was chosen for further study due to its more desirable properties in TPL and estimated T_g.

B. Triacrylate Resin

Optimizing Microstructures from Two-Photon Lithography

A SMP photoresist for two-photon lithography (TPL) was created using poly(benzyl methacrylate) (pBMA), FMA, and functionalized pentaerythritol triacrylate (PETA). PETA was functionalized with 2-(boc-amino) ethanethiol in a 1:1 molar ratio, yielding two unreacted acrylate groups for polymerization. Proper functionalization of components was confirmed via ^{1}H NMR by Elliott et al.[12] Resists made with as-received benzyl methacrylate experienced boiling during TPL, making it impossible to print microstructures. To prevent this, the BMA was partially polymerized under UV for 4 minutes prior to incorporation into the resist, creating pBMA oligomers with a higher boiling temperature that did not cause issues during printing.

SMP microstructures were written using TPL onto a functionalized silicon chip by a femtosecond laser in slices from bottom to top. Each section was written by outlining the cross section at a given height and filling in the center with parallel lines. This process can be tuned by altering writing parameters, including laser power, laser scan speed, hatching distance (the spacing between lines in cross-sectional slices), and the z-slice distance (the vertical spacing between slices). Multiple sets of writing conditions within this parameter space successfully yielded microstructures, which differ in their physical forms despite being created from the same 3D model (Figure 6). In general, very small hatching and z-slice distances caused overexposure, resulting in explosions and misshapen structures, while larger hatching and z-slice distances resulted in shrinkage, which likely occurred during development. Optimizing for both the form of structures

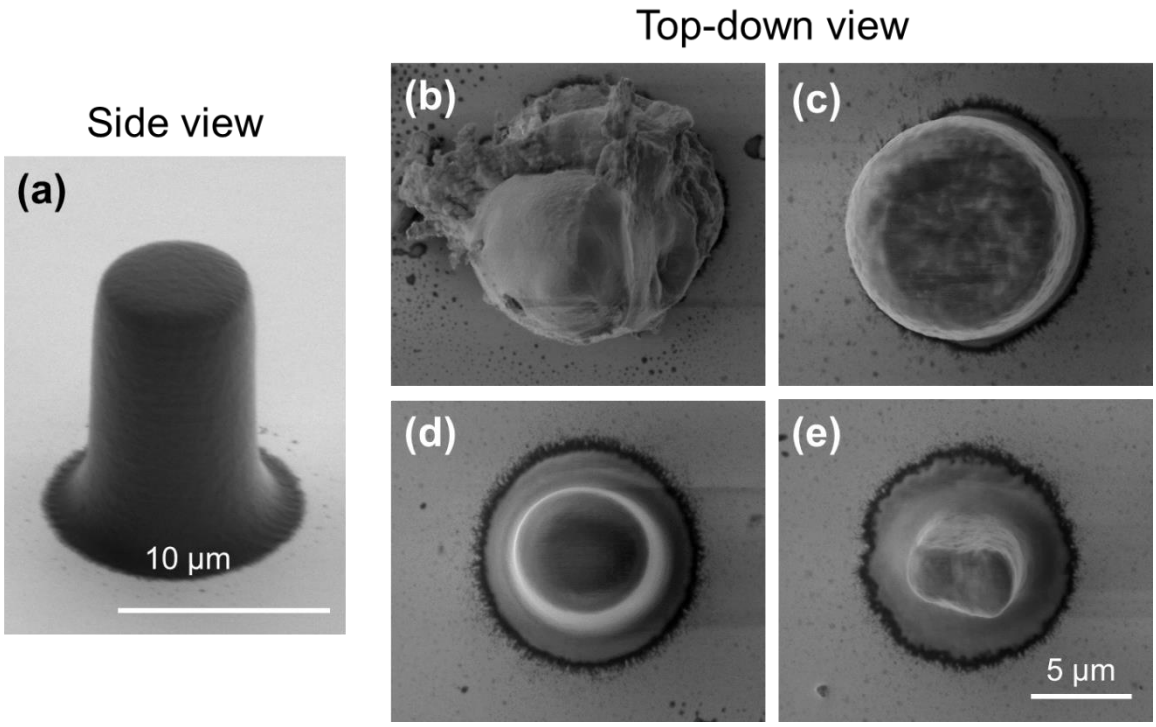

Figure 6. Microscale pillars fabricated under different slicing conditions. (a) Side view of pillar with writing conditions shown in panel (d). The following panels show top-down views of pillars of intended diameter 10 µm that were fabricated at equal laser power and scan speed and z-slice and hatching distances of (b) 50 nm and 25 nm; (c) 50 nm and 50 nm; (d) 150 nm and 50 nm; and (e) 150 nm and 100 nm. Very small hatching distances tended to cause overexposure as seen in (b), while increasing z-slice and hatching distances increased the appearance of shrinkage, as seen in (d) and (e) compared to (c).

and the time taken to print structures, the standard writing conditions used were the following: z-slice: 100 nm, hatching: 50 nm, laser power: 25 mW, scan speed: 2500 µm s^{-1}.

Mechanical Characterization of Microstructures

The SMP microstructures underwent mechanical characterization via dynamic nanomechanical analysis and displayed shape memory cycling in *in-situ* temperature-controlled compression experiments described in Elliott et al.[12] These topics will not be treated in depth here, but a summary of key information obtained is presented. The SMP microstructures displayed a sharp decrease in storage stiffness and an increase in tangent delta within the temperature range of

60 °C to 87 °C, indicating that the onset of shape change begins at approximately 60 °C. This is consistent with the location of the peak in loss stiffness around 77 °C, indicating an approximate value for T_g.

The microstructures also underwent shape memory cycles in which pillars were pressed downwards by an indenter tip at 77 °C and cooled to 42 °C while maintaining compressive load. After 30 minutes of holding the compressed, temporary shape without external load, the temperature was raised to 87 °C, allowing the structures to recover to their original shapes (Figure 7). Using an equation analogous to Eq. 2 with the metric of height rather than angle, the structures were determined to have shape recovery values of 86 ± 4%.

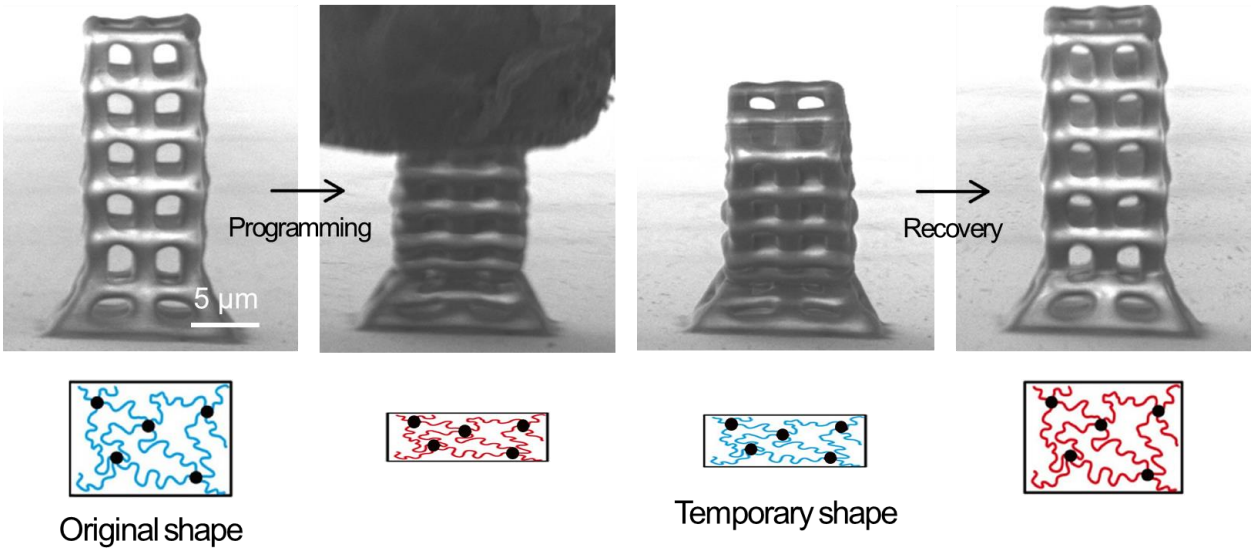

Figure 7. Shape memory cycles undergone by SMP micro lattices. Microstructures readily exhibit shape memory cycling in *in-situ* compressive experiment with change in height used to quantify shape recovery. SEM images courtesy of Luizetta Elliott.

Functional Group Identification via Raman Spectroscopy

Differences between microstructures with different writing parameters were conjectured to be linked to different degrees of polymerization and possibly the relative incorporation of each

component into the final microstructures. To understand these network properties, Raman spectroscopy was performed to identify the functional groups present in the resin as well as the individual resin components.

Raman spectroscopy detects the inelastic scattering, or Raman scattering, of monochromatic laser light. In this type of scattering, incident light excites electrons in the material being examined to a higher energy virtual state; however, when the electron falls out of this excited state, it returns to a vibrational level different from the one it was in before excitation, causing the emitted light to have a different energy and therefore different wavelength than the incident light. The difference in wavelength of the incident light (λ_0) and that of the emitted light (λ_1) determine the Raman shift (Δw), which is usually expressed in wavenumbers, as follows:

$$\Delta w = \left(\frac{1}{\lambda_0} - \frac{1}{\lambda_1}\right) \qquad (3)$$

In polymers and other materials, functional groups undergo Raman scattering at characteristic Raman shifts, creating a peak on a graph of intensity versus Raman shift, allowing for functional group identification.

Raman data in the range of Raman shifts 800-1800 cm^{-1} was taken for all components used in the resist before and after pre-polymerization or functionalization, as well as the resin itself as a liquid, a macroscale sample polymerized by UV, and in microstructures with different TPL writing conditions. A representative spectrum for the complete resin in its two polymerized forms with peaks identified is shown in Figure 8.[13–15] Note that the aliphatic C=C peak at 1635 cm^{-1} is not clearly visible in these spectra, as the samples are polymerized and likely have very few unreacted aliphatic C=C bonds.

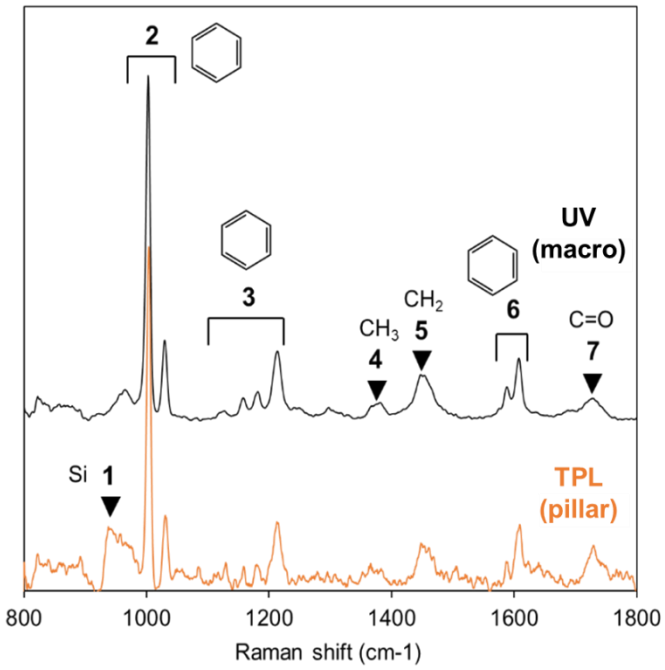

#	Wavenumber (cm^{-1})	Feature
1	940-960	Silicon chip
2	1004, 1030	Ring breathing, deformation (in-plane)
3	1130-1215	Ring deformation (in-plane)
4	1370-1380	CH_3 symmetric bending
5	1450	CH_2 scissoring
6	1585, 1605	Aromatic C=C stretching
-	1635	Aliphatic C=C stretching
7	1730	C=O stretching

Figure 8. Typical Raman spectrum with peaks identified. Note that the aliphatic C=C peak at 1635 cm^{-1} is not clearly visible in these spectra, as they are polymerized and most likely have very few unreacted aliphatic C=C bonds.

Raw Raman data underwent two treatments to obtain the signals used for peak analysis: smoothing and baseline correction. The smoothing function, `smooth`, utilizes a moving average filter; the baseline correction function, `msbackadj`, uses a shape preserving piecewise cubic interpolation regression method to determine the shape of the baseline, which is then subtracted from the signal. The MATLAB program and the results of these treatments are shown in Figure S2. Peaks were identified and their locations, intensities, and widths (FWHM) calculated using the `findpeaks` function, and the area under these peaks are calculated using the trapezoid numerical integration method.

Figures 9a and 9b compare the spectra of the as received versus functionalized methacrylate chain builder and PETA. The most informative difference between the two sets of spectra is the increased prominence of bands at ~1370 cm^{-1} after functionalization, which

corresponds to the great increase in methyl groups introduced through the BOC protecting groups. The increased intensity of the peaks from 800-1200 cm^{-1} after functionalization can likely be attributed to the lengthening of the chains in both molecules due to functionalization, as these peaks are characteristic of straight chain and branched alkanes. The increased prominence of peaks at ~1450 cm^{-1} is likely due to the increase in methylene groups. The ratio of the aliphatic C=C stretching band (1635 cm^{-1}) and the C=O stretching band (1730 cm^{-1}) increased slightly after functionalization in both compounds, possibly reflecting the addition of the amine. Overall, these data suggest that functionalization of both compounds was successful.

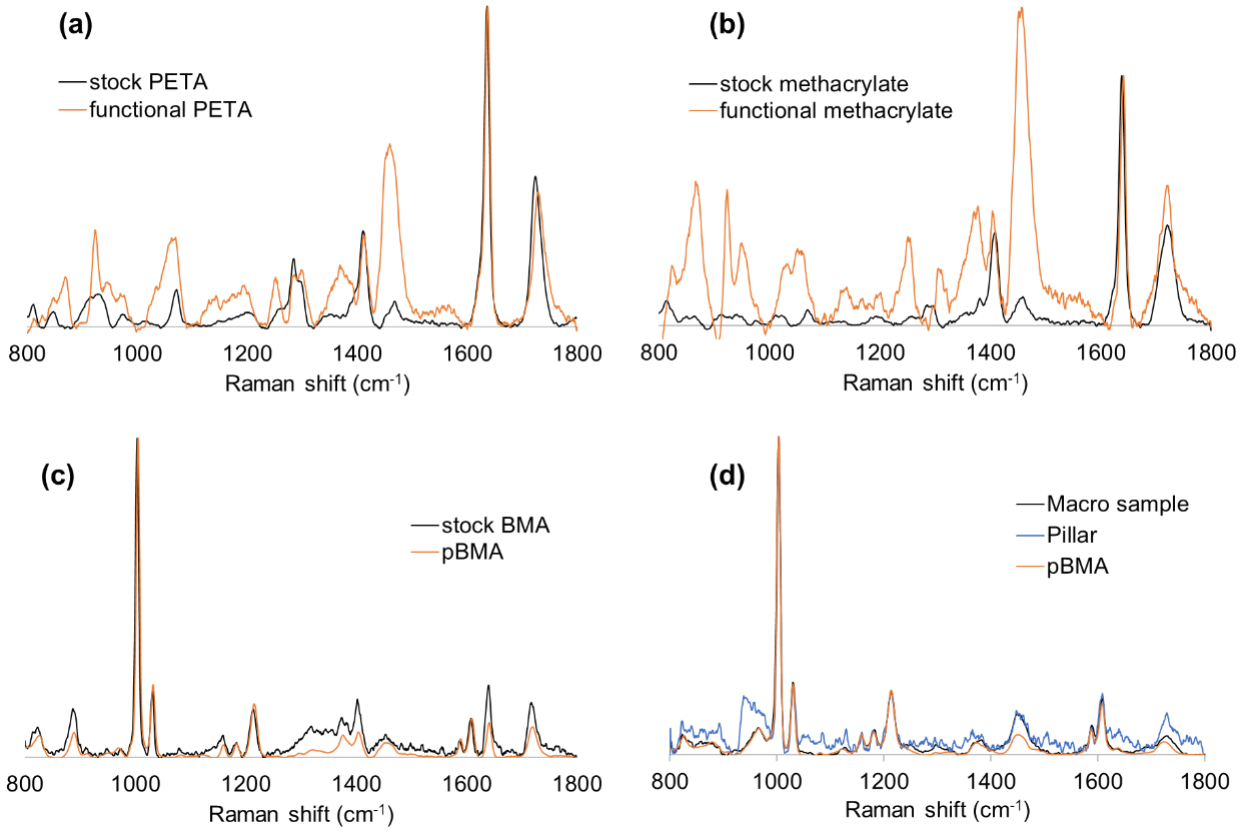

Figure 9. Comparison of Raman spectra for (a) crosslinker (stock and functionalized) (b) methacrylate chain builder (stock and functionalized), (c) BMA (stock and pre-polymerized), and (d) pBMA and polymerized samples of the full resin. The pillar used in (d) was written at laser power 25 mW, scan speed 2500 µm s^{-1}, hatching distance 50 nm, and z-slice 100 nm. Intensity on the y-axis has arbitrary units.

Figure 9c compares the spectra of as received and pre-polymerized BMA. The primary point of interest in this comparison is the decrease in the ratio of the areas under the aliphatic C=C band (1635 cm^{-1}) to the aromatic C=C band (1605 cm^{-1}). This suggests that the pBMA used was a mixture of monomers and oligomers as intended. More discussion of the degree of polymerization will follow in the next section.

Comparing the spectra of the pBMA with the fully polymerized resin (Figure 9d), there are very few differences with the notable exception of the CH_2 scissoring band (1450 cm^{-1}). This indicates that the final structures contain pBMA and likely some of the other components, which contribute to the CH_2 band. However, with no direct evidence for the presence of amine groups in the final resin, other methods were used to confirm their incorporation into the final structures (see Amine Group Chemistry section following).

Degree of Polymerization Calculations

In past works, Raman spectroscopy has been used to calculate degree of polymerization by comparing the relative prevalence of aliphatic C=C bonds before and after polymerization to that of another functional group that should remain unaltered during the polymerization process, including benzene rings and carbonyls.[14–17] Approximate degrees of polymerization (DP) for pBMA and the full resin in the macroscale samples and pillars were calculated using the following formulas:

$$DP\ \% = \left(1 - \frac{R_{polymer}}{R_{resin}}\right) \cdot 100 \qquad (4)$$

$$R = \frac{A_{aliphtic\ C=C}}{A_{C=O}} \quad \text{or} \quad R = \frac{A_{aliphatic\ C=C}}{A_{aromatic\ C=C}} \qquad (5, 6)$$

where A_X is the area under the Raman peak associated with the functional group X. Note that the second formula for the ratio *R* using aromatic C=C bonds could not be used for the methacrylate chain builder and PETA.

This method did not have great success for the pillars printed using TPL due to the low intensity of the peaks relative to the noise in the data. The degree of polymerization data obtained was quite inconsistent with data taken for a single pillar and between methods (aromatic C=C and C=O) and showed no discernable trends between writing conditions. Thin plates (3 μm thickness) with large cross-sectional areas were also tested and showed no improvement on the previous data. This implies that the depth resolution of the instrument was likely larger than the height of the pillars (15 μm), making data collection for these microstructures difficult. DP values obtained are included in Table S2.

Degree of polymerizations calculations were made for pBMA and a sample of BMA that was polymerized under UV light until it was completely solid (~1 hour) using the C=C aromatic group as a reference, giving 45 ± 3% and 89 ± 0.3%, respectively.

C. Exploring Functionality

Amine Group Chemistry

In addition to controlling the architecture of 3D microstructures, incorporating surface functionality into the structures can help to expand their potential applications. One approach to incorporate functionality into microstructures is to add functional nanoparticles into the resist prior to structure fabrication.[18] However, it is difficult to disperse nanoparticles in viscous resists, and aggregation of the particles can make the resin opaque to laser light, hindering lithography. Another approach involves using any unreacted groups at the end of polymer chains near the surface of the structure to add functional groups. However, very few of these unreacted groups

usually remain after polymerization. In a thiol-ene resin, Quick et al. showed that the density of unreacted thiol groups available on the surface was ~200 molecules μm^{-2}.[19]

In this system, the addition of BOC-protected amine groups to the resin components prior to fabrication creates no barrier to TPL and can also yield many available groups on the structures' surfaces. In the similar polymer system created by Yee et al., the structures had a surface density of accessible amine groups of $3.9 \pm 0.7 \times 10^8$ molecules μm^{-2}.[8]

To confirm that the polymer microstructures were properly functionalized, the amine groups were dyed using Orange II sodium salt, which can be seen with the unaided eye, following a process similar to those in previous works.[8,20] To access the amine groups on the structures' surface, the BOC-protecting groups were removed from the amines via acid deprotection. The deprotected structures were then submerged in a solution containing Orange II sodium salt, dyeing

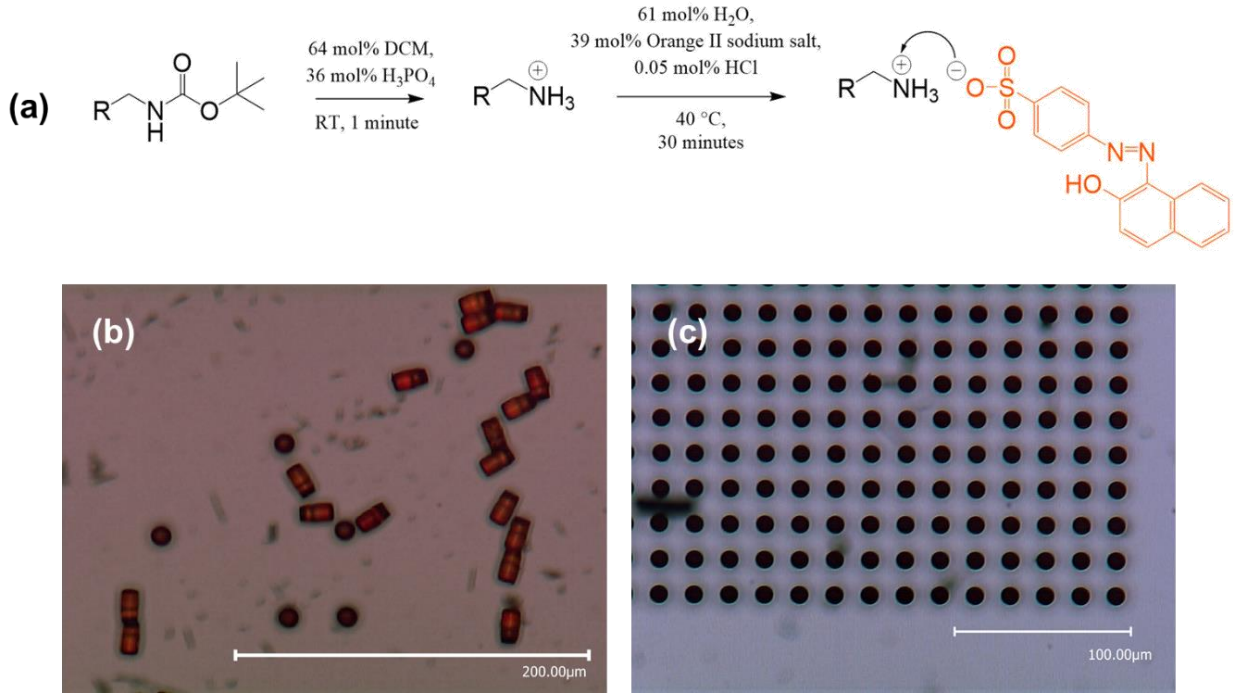

Figure 10. Orange II attachment. (a) Deprotection and Orange II addition reaction schemes. (b) Pillars underwent Orange II dyeing but were easily detached from the silicon chip surface. (c) Future chips were functionalized to help pillars remain upright after the reaction.

the structures orange (Figure 10). Despite the success of the Orange II attachment, the density of available amines was not measured for this system. The structures printed did not provide enough surface to attach a quantifiable amount of Orange II dye, but the visible orange color demonstrates that surface amines were available for functionalization.

Gold Nanoparticle Functionalization for Remote Heating.

In biomedical applications, heating SMP structures to the appropriate temperatures to induce shape change may pose some risk to the patient if the surrounding tissues are also heated to high temperatures. To combat this, the SMP system can be altered with added functionality to allow for heating a specific target area from a distance. One such method is to incorporate gold nanoparticles (AuNPs) into the polymer; AuNPs in a range of sizes and morphologies are known to undergo photothermal heating via localized surface plasmon resonance (LSPR). LSPR is a phenomenon that occurs when light interacts with conductive nanoparticles (NPs) that are smaller than the incident wavelength. This interaction causes an excitation of electrons in the conduction band of the NPs, resulting in oscillations with a particular resonant frequency depending on the size and shape of the NP. When exposed to laser light with a wavelength corresponding to this resonant frequency, the absorption by the NP is greatly enhanced, resulting in heating of the surrounding medium, which has the potential to give rise to shape change in an SMP.

One way to achieve this affect in SMPs is to incorporate AuNPs into the polymer resin itself before polymerization.[21,22] However, this approach would hinder laser penetration through the photoresist during TPL, hindering the writing of structures. Rather than adding the AuNPs to the photoresist, in this SMP system, AuNPs can be attached to the surface of microstructures via the amine functional groups after fabrication. This is accomplished by deprotecting the amine groups on the polymer surface and reacting the amines with anhydride groups in S-

acetylmercaptosuccinic anhydride (SAMSA).[23] AuNPs can then be bound to the structures via their affinity to mercapto groups that can be exposed by deprotection of the bound SAMSA.[24,25] This procedure was described and initially carried out by Abadi et al.; spherical AuNPs of diameter 40 nm were attached to disks (7.9 mm diameter, 0.6 mm thickness) of the same SMP polymer system.[26] This work showed that attaching AuNPs to the surface of the polymer and exposing to laser light of wavelength 532 nm causes shape change, whereas laser light alone with no AuNPs present does not. These results indicate promise for remotely induced shape change microstructures, and while these experiments were not performed, this possibility was given a theoretical treatment.

Heat Transfer in Theoretical Pillar System

First, an estimation of the temperature change in each AuNP due to LSPR at λ = 532 nm was made. This was done in accordance with Mie theory, which is a solution to Maxwell's equations describing the scattering of plane electromagnetic waves by a sphere of any size and any refractive index.[27,28] The absorbance cross section (σ_{abs}) of a particle with radius *r* is calculated from the cross sections of total extinction (σ_{ext}) and scattering (σ_{sca}) through the following equations:

$$\sigma_{ext} = \frac{2\pi}{k^2}\sum_{n=1}^{\infty}(2n+1)\,\mathrm{Re}[a_n + b_n] \qquad (7)$$

$$\sigma_{sca} = \frac{2\pi}{k^2}\sum_{n=1}^{\infty}(2n+1)[a_n^2 + b_n^2] \qquad (8)$$

$$\sigma_{abs} = \sigma_{ext} - \sigma_{sca} \qquad (9)$$

$$a_n = \frac{m\psi_n(mv)\psi_n'(v) - \psi_n(v)y_n'(mv)}{m\psi_n(mv)\xi_n'(v) - m\xi_n(v)\psi_n'(mv)} \qquad (10)$$

$$b_n = \frac{\psi_n(mv)\psi_n'(v) - m\psi_n(v)\psi_n'(mv)}{\psi_n(mv)\xi_n'(v) - m\xi_n(v)\psi_n'(mv)} \qquad (11)$$

where m is the ratio of refractive index of the nanoparticle n to that of the surrounding medium n_m, k is given by $2\pi n_m/\lambda$, v is given by $k \cdot r$, and ψ_n and ξ_n are the Riccati-Bessel functions. Note that here, the index of refraction for the medium is taken to be the average between that of air and poly(methyl methacrylate) (PMMA). Note that Mie theory cannot account for the refractive indices of multiple media. The averaging approach was shown to yield values consistent with empirical values found for a single particle in contact with air and glass substrate.[29] This simplification does not account for the contributions of more complex multi-particle interactions. The refractive index of PMMA at 532 nm is used for the substrate because it is the most chemically similar compound for which this parameter is readily available. This value could be measured for the SMP resin itself experimentally using a refractometer.

From the absorption cross section, we can calculate the change in temperature that the nanoparticles will undergo due to LSPR:

$$\delta T = \frac{\sigma_{abs} I}{4\pi\kappa_s r} \qquad (12)$$

where I is light irradiance (power per unit area) and κ_m is the thermal conductivity of the medium. Here, the medium thermal conductivity is taken as the average of that of the two media (air and PMMA), as this is a valid assumption for particles sitting on the surface of a substrate. The code used for these calculations is adapted from Baffou et al. and can be found in Figure S3.[27]

For a laser setup with a max power of 6 W and a minimum spot size diameter of 200 μm, the calculated change in temperature for the nanoparticles is approximately 16.8 °C. This calculated temperature ignores multi-particle interactions and the distribution of the AuNP, which

could alter the distribution of temperature across the surface of the structure.[30] However, this calculation was outside the scope of the project.

This increase in temperature was assumed to be equal to the temperature increase of the surface of a SMP structure to find steady state temperatures within the pillar. Ideally, temperatures within the pillar should reach T_g to induce shape change in the structure. When steady state is obtained, the heat flow generated by LSPR ($\dot{q}$) should be balanced by heat removal into the pillar and into the air. This can be written simply as:

$$\dot{q} = \kappa \frac{dT}{dx} + h(T_s - T_{bulk}) \qquad (13)$$

where κ is thermal conductivity, $\frac{dT}{dx}$ is the thermal gradient in the pillar, h is the heat transfer coefficient for convection, T_s is the temperature of the nanoparticles, and T_{bulk} is the temperature of the surrounding air.[31] However, a complete picture of this system must include the silicon chip beneath the pillar, which acts as a heat sink, introducing another layer of complexity into the calculation.

Solving this system numerically would become cumbersome, so the finite element analysis software COMSOL was used to sketch temperature profiles for the inside and surroundings of the pillar. The simulation done used physics for 3D heat transfer in solids, and the stationary solution was calculated to give steady state temperature profiles. The pillar was modeled as a PMMA cylinder with diameter 10 μm and height 15 μm. The temperature of the top and sides of the pillar was set to a constant 42 °C, and the bottom was set to 25 °C, representing the interface with the silicon chip, which should conduct heat away from the pillar relatively well compared to air. The air around the pillar was modeled by a cube with side length 30 μm. The temperature at all boundaries of the cube was set to 25 °C, representing the bulk temperature of the air some distance

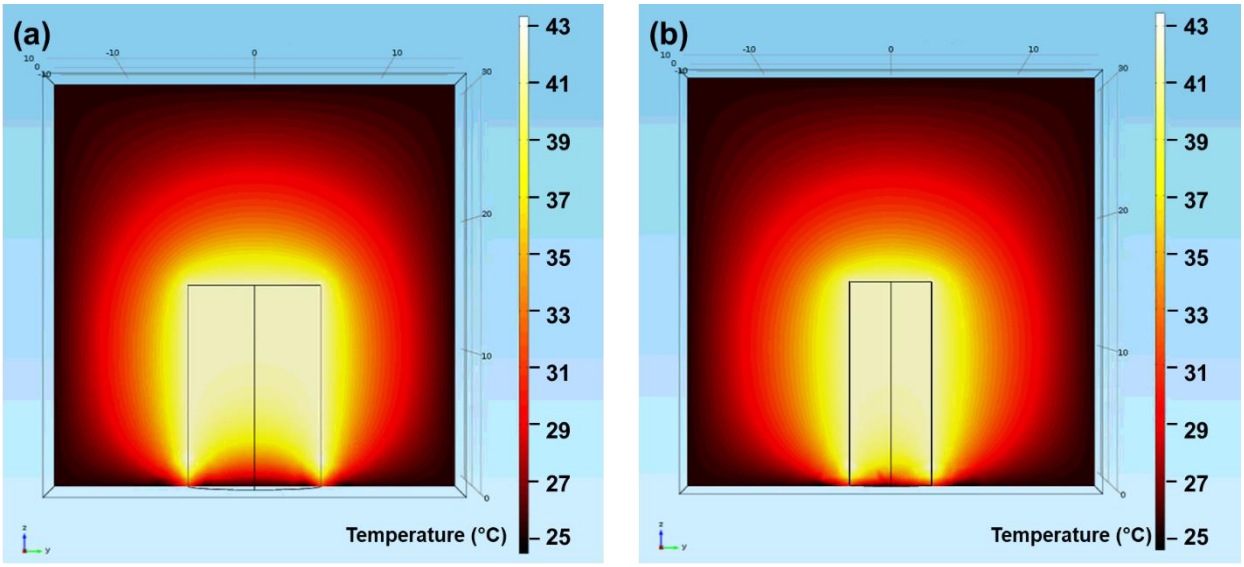

Figure 11. COMSOL simulation images for temperature distribution in pillar. Images taken are slices through (a) the pillar diameter and (b) 4 μm offset from the diameter. The small, dark outlined rectangles are the pillar, and the large square surrounding them is boundary of the air modeled around the pillar.

away from the pillar (but not close to another AuNP-coated feature that may be part of a more complex overall geometry in the microstructure, e.g. another strut in a lattice). This distance would need to be tuned for larger, more complex geometries, but should not greatly affect the temperatures calculated within the cylinder.

The calculated temperature profiles within the cylinder are shown in Figure 11. These profiles show that the interior throughout the upper three quarters of the pillars stay at or above approximately 37 °C, which is a 12 °C increase over the surrounding air. Although this temperature may not be high enough to induce shape change in this particular resin composition, this substantial temperature change extends all the way to the core of the pillars, meaning that the approach of coating a structure in AuNPs rather than incorporating them into the resist still presents a viable method of inducing shape change in a microstructure. The bottom quarter of the pillar experiences lower temperature than the rest of the pillar, indicating that shape recovery may not be easily

achieved near a substrate that has high thermal conductivity. This would need to be considered in applications where there is a large surface area interface with a heat conducting substrate.

Additionally, phenomena not addressed in this simulation, including more complex interaction between NPs and their distribution on the microstructure surface, may change temperature distribution in the system. This possibility warrants a more sophisticated look at heat generation by the surface AuNPs to obtain a more complete picture of the system.

IV. Conclusion

The BMA-based SMP resin described here has been adapted into a photoresist that can be used to create complex 3D microarchitectures via two-photon lithography that exhibit shape memory cycling capabilities around the glass transition. The composition of these structures was explored using Raman spectroscopy to gain insight that could not be had through more common techniques like solid state NMR due to the small amount of sample created by the fabrication technique used. Additionally, the rapid bending test created to identify promising SMP compositions for TPL resist development revealed trends in shape memory traits based on crosslinker concentration and relative ratios of different chain builders in the system. These trends are consistent with intuition and could be useful in future resin development.

These SMP structures are also outfitted with BOC-protected amine groups, granting added functionality to the microstructures. This functionality opens a variety of possibilities for enhancing microstructure applications, including the attachment of AuNPs that exhibit thermoplasmonic heating for remote activation of shape recovery. In preliminary calculations for a model system, AuNPs yielded a surface temperature change in the microstructures of nearly 18 °C, which could readily be utilized to induce shape recovery. The amine functionality in the

SMPs could also be used in other ways that have yet to be explored, including conjugating to proteins in biological systems for better adhesion. Overall, this work offers a potentially impactful new material that could be tuned for use in systems, both biological and not, that require small scale, stimuli responsive shape changes.

V. Experimental

Materials: Pentaerythritol triacrylate (PETA) (technical grade, Sigma Aldrich), dipentaerythritol pentaacrylate (DPEPA) (low viscosity, Sartomer), 3-(acryloyloxy)-2-hydroxypropyl methacrylate (Sigma Aldrich), benzyl methacrylate (BMA) (96%, Sigma Aldrich), 2-(boc-amino) ethanethiol (97%, Sigma Aldrich), hexylamine (99%, Sigma Aldrich), ethyl phenyl (2,4,6-trimethylbenzoyl) phosphinate (TPO-L) (Rahn USA Corp.), silicone elastomer base and curing agent (Sylgard), acetic acid (≥99%, Sigma Aldrich), ethyl alcohol (95%, Koptec), 3-(trimethoxysilyl)propyl methacrylate (98%, Sigma Aldrich), 7-dimethylamino-3-thenoylcoumarin (DETC) (Exciton), propylene glycol monomethyl ether acetate (PGMEA) (>99.5%, Sigma Aldrich), isopropyl alcohol (IPA) (99.7%, Sigma Aldrich), dichloromethane (DCM) (>99%, Alfa Aesar), phosphoric acid (85%, Alfa Aesar), sodium bicarbonate (>99.7%, Sigma Aldrich), Orange II sodium salt (>85%, Sigma Aldrich), and hydrochloric acid (36.5-38%, J. T. Baker) were used without further purification.

Synthesis of functionalized chain builder and crosslinkers via Thiol-Michael reactions: To functionalize the methacrylate chain builder, 3-(acryloyloxy)-2-hydroxypropyl methacrylate (1.0 equiv., 1.1 mL) and 2-(boc-amino) ethanethiol (1.0 equiv., 1 mL) were combined by stirring in an ice bath. The mixture was then removed from the ice bath and catalyzed with hexylamine (0.1

equiv., 156 µL) added dropwise. The solution was stirred for 30 minutes until the mixture was noticeably more viscous.

To functionalize the crosslinkers, PETA (1.0 equiv., 189 µL) or DPEPA (1.0 equiv., 62 µL) and 2-(boc-amino) ethanethiol (1 equiv., 126 µL with PETA, 23 µL with DPEPA) were combined and catalyzed with hexylamine (0.1 equiv.) using the same methods as the chain builder.

Pre-polymerization of BMA: Small quantities of BMA (500 µL) were combined with TPO-L (7 µL) and polymerized under a UV lamp (36 W, DR-301C, MelodySusie) for 4 minutes while stirring vigorously in a vial on a stir plate. Vials containing the pBMA were then immediately submerged in an ice bath for 2 minutes to slow polymerization reactions and wrapped in foil for storage.

Macroscale sample synthesis and polymerization: Aliquots of FMA, pBMA, and functionalized PETA or DPEPA resin (170 µL) were combined with TPO-L (7 µL) and cured for 1 hour under UV light.

Creation of polydimethylsiloxane (PDMS) molds: Silicone elastomer base and curing agent were combined in a 10:1 mass ratio and mixed vigorously until the mixture appeared milky white due to trapped air bubbles. The mixture was degassed under vacuum, poured into 3D-printed polylactic acid (PLA) mold boxes, and degassed again. The molds were then cured at 65 °C until firm (~12 hours) before being removed from the mold boxes.

Photoresist preparation for TPL: To formulate the resist for lithography, FMA (0.3 mL), pBMA (1.2 g), and PETA (336 µL) were combined and stirred for several hours up to overnight. The pBMA was added by mass rather than volume due to its high viscosity and resulting difficulty in pipetting. A solution of the photoinitiator DETC (4.5 mg) was dissolved in DCM (20 µL) and

combined with 200 µL of the resin mixture. The resist was stirred, wrapped in aluminum foil, and refrigerated for storage.

Functionalization of silicon chips: Silicon chips were ultrasonicated in IPA for 20 minutes and dried with argon. A solution of 95% ethanol and 5% water was adjusted to an approximate pH of 5 with acetic acid. 3-(Trimethoxysilyl)propyl methacrylate was added with stirring to obtain a 2% final concentration. The silicon chips were then dipped in the solution for 1 minute and cured at 110 °C for 8-10 minutes.

Two-Photon Lithography of polymer resins and Scanning Electron Microscopy imaging: TPL was performed using the Photonic Professional GT, Nanoscribe GmbH system using 30 mm diameter circular glass slides and functionalized 10 mm x 10 mm silicon chips. Photoresist (~5 µL) was drop cast onto a 30 mm diameter 0.17 mm thick glass slide. A functionalized silicon chip was then placed over the glass slide and adhered with Kapton tape. Unless otherwise noted, the structures were written via TPL with 30 mW laser power, 2000 $cm \cdot s^{-1}$ scan speed, 50 nm hatching distance, and 100 nm slices. The structures were developed in PGMEA for 1 hour, IPA for 1 hour, and filtered IPA for 30 minutes. Structures were critical point dried (Autosamdri 931.GL, Tousimis Research Corporation).

SEM images were performed in a combination scanning electron microscope and nanoindenter (InSEM; Nanomechanics and FEI Quanta 200).

Raman spectroscopy on macroscale and microscale samples: Raman spectra were collected for both macroscale samples and TPL microstructures using a Renishaw confocal Raman microscope with 783.7 nm incident laser radiation. All spectra were obtained in five accumulations, each spanning 10 seconds to minimize levels of noise to signal. Solid, polymerized samples were

measured directly. For liquids, one drop of each sample was sandwiched between two glass slides separated by a layer of Kapton tape for measurement.

Deprotection and Orange II Amine dying: Samples were placed in a solution of DCM (3 mL) and phosphoric acid (1.5 mL) for 1 minute. The samples were rinsed with water and neutralized in a bath of water and sodium bicarbonate. The samples were then placed in a solution of water (5 mL), hydrochloric acid (7.5 µL), and Orange II sodium salt (62.8 mg) at 40 °C for 1 hour. The samples were then rinsed with water adjusted to pH 3 with HCl to remove excess dye and dried with argon.

To remove dye bound to the structures for quantification, the samples were placed in water adjusted to pH 12 with NaOH at 40 °C for between 2 and 5 hours. The solution containing the desorbed dye was then adjusted to pH 3 using HCl. The absorbance of the solution was measured at 480 nm using an Agilent 8453 UV-visible spectrophotometer and correlated with the concentration of Orange II using a calibration curve.

VI. Acknowledgements

This work was supported by funding from the David S. Koons and Arthur R. Adams fellowships through Caltech's Student-Faculty Programs office.

The author would like the thank Luizetta Elliott, who operated the Nanoscribe and served as an exceptional mentor throughout this project. The author also thanks Dr. Julia Greer for her support, guidance, and feedback.

The author also acknowledges Dr. George Rossman for use of the Raman spectrometer and for his assistance with this technique. The author is also grateful to Daryl Yee for his support with

synthesis and two photon lithography and Andrew Friedman for his guidance on heat transfer topics and COMSOL modeling.

VII. References

(1) Zhao, Q.; Qi, H. J.; Xie, T. Recent Progress in Shape Memory Polymer: New Behavior, Enabling Materials, and Mechanistic Understanding. *Prog. Polym. Sci.* **2015**, *49–50*, 79–120. https://doi.org/10.1016/j.progpolymsci.2015.04.001.

(2) Liu, C.; Qin, H.; Mather, P. T. Review of Progress in Shape-Memory Polymers. *J. Mater. Chem.* **2007**, *17* (16), 1543–1558. https://doi.org/10.1039/B615954K.

(3) Chan, B. Q. Y.; Low, Z. W. K.; Heng, S. J. W.; Chan, S. Y.; Owh, C.; Loh, X. J. Recent Advances in Shape Memory Soft Materials for Biomedical Applications. *ACS Appl. Mater. Interfaces* **2016**, *8* (16), 10070–10087. https://doi.org/10.1021/acsami.6b01295.

(4) Yakacki, C. M.; Gall, K. Shape-Memory Polymers for Biomedical Applications. In *Shape-Memory Polymers*; Lendlein, A., Ed.; Advances in Polymer Science; Springer: Berlin, Heidelberg, 2010; pp 147–175. https://doi.org/10.1007/12_2009_23.

(5) Ge, Q.; Sakhaei, A. H.; Lee, H.; Dunn, C. K.; Fang, N. X.; Dunn, M. L. Multimaterial 4D Printing with Tailorable Shape Memory Polymers. *Sci. Rep.* **2016**, *6* (1), 31110. https://doi.org/10.1038/srep31110.

(6) Baldacchini, T. *Three-Dimensional Microfabrication Using Two-Photon Polymerization: Fundamentals, Technology, and Applications*; William Andrew, 2015.

(7) Mao, M.; He, J.; Li, X.; Zhang, B.; Lei, Q.; Liu, Y.; Li, D. The Emerging Frontiers and Applications of High-Resolution 3D Printing. *Micromachines* **2017**, *8* (4), 113. https://doi.org/10.3390/mi8040113.

(8) Yee, D. W.; Schulz, M. D.; Grubbs, R. H.; Greer, J. R. Functionalized 3D Architected Materials via Thiol-Michael Addition and Two-Photon Lithography. *Adv. Mater.* **2017**, *29* (16), 1605293. https://doi.org/10.1002/adma.201605293.

(9) Li, F.; Larock, R. C. New Soybean Oil–Styrene–Divinylbenzene Thermosetting Copolymers. v. Shape Memory Effect. *J. Appl. Polym. Sci.* **2002**, *84* (8), 1533–1543. https://doi.org/10.1002/app.10493.

(10) Safranski, D. L.; Gall, K. Effect of Chemical Structure and Crosslinking Density on the Thermo-Mechanical Properties and Toughness of (Meth)Acrylate Shape Memory Polymer Networks. *Polymer* **2008**, *49* (20), 4446–4455. https://doi.org/10.1016/j.polymer.2008.07.060.

(11) Chan, J. W.; Hoyle, C. E.; Lowe, A. B.; Bowman, M. Nucleophile-Initiated Thiol-Michael Reactions: Effect of Organocatalyst, Thiol, and Ene. *Macromolecules* **2010**, *43* (15), 6381–6388. https://doi.org/10.1021/ma101069c.

(12) Elliott, L. V.; Salzman, E.; Greer, J. R. Stimuli Responsive Shape Memory Micro-Architectures (Under Review). **2020**.

(13) Socrates, G. *Infrared and Raman Characteristic Group Frequencies: Tables and Charts*; John Wiley & Sons, 2004.

(14) E. Barnes, S.; T. Cygan, Z.; K. Yates, J.; L. Beers, K.; J. Amis, E. Raman Spectroscopic Monitoring of Droplet Polymerization in a Microfluidic Device. *Analyst* **2006**, *131* (9), 1027–1033. https://doi.org/10.1039/B603693G.

(15) Jiang, L. J.; Zhou, Y. S.; Xiong, W.; Gao, Y.; Huang, X.; Jiang, L.; Baldacchini, T.; Silvain, J.-F.; Lu, Y. F. Two-Photon Polymerization: Investigation of Chemical and Mechanical Properties of Resins Using Raman Microspectroscopy. *Opt. Lett.* **2014**, *39* (10), 3034–3037. https://doi.org/10.1364/OL.39.003034.

(16) Shin, W. S.; Li, X. F.; Schwartz, B.; Wunder, S. L.; Baran, G. R. Determination of the Degree of Cure of Dental Resins Using Raman and FT-Raman Spectroscopy. *Dent. Mater.* **1993**, *9* (5), 317–324. https://doi.org/10.1016/0109-5641(93)90050-Z.

(17) Khalil, S. K. H.; Allam, M. A.; Tawfik, W. A. Use of FT-Raman Spectroscopy to Determine the Degree of Polymerization of Dental Composite Resin Cured with a New Light Source. *Eur. J. Dent.* **2007**, *01* (2), 72–79. https://doi.org/10.1055/s-0039-1698317.

(18) Sun, Z.-B.; Dong, X.-Z.; Chen, W.-Q.; Nakanishi, S.; Duan, X.-M.; Kawata, S. Multicolor Polymer Nanocomposites: In Situ Synthesis and Fabrication of 3D Microstructures. *Adv. Mater.* **2008**, *20* (5), 914–919. https://doi.org/10.1002/adma.200702035.

(19) Quick, A. S.; Fischer, J.; Richter, B.; Pauloehrl, T.; Trouillet, V.; Wegener, M.; Barner-Kowollik, C. Preparation of Reactive Three-Dimensional Microstructures via Direct Laser Writing and Thiol-Ene Chemistry. *Macromol. Rapid Commun.* **2013**, *34* (4), 335–340. https://doi.org/10.1002/marc.201200796.

(20) Noel, S.; Liberelle, B.; Robitaille, L.; De Crescenzo, G. Quantification of Primary Amine Groups Available for Subsequent Biofunctionalization of Polymer Surfaces. *Bioconjug. Chem.* **2011**, *22* (8), 1690–1699. https://doi.org/10.1021/bc200259c.

(21) Zhang, H.; Xia, H.; Zhao, Y. Optically Triggered and Spatially Controllable Shape-Memory Polymer–Gold Nanoparticle Composite Materials. *J. Mater. Chem.* **2011**, *22* (3), 845–849. https://doi.org/10.1039/C1JM14615G.

(22) Zheng, Y.; Li, J.; Lee, E.; Yang, S. Light-Induced Shape Recovery of Deformed Shape Memory Polymer Micropillar Arrays with Gold Nanorods. *RSC Adv.* **2015**, *5* (39), 30495–30499. https://doi.org/10.1039/C5RA01469G.

(23) Hermanson, G. T. *Bioconjugate Techniques*; Academic Press, 2013.

(24) Cannone, F.; Chirico, G.; Bizzarri, A. R.; Cannistraro, S. Quenching and Blinking of Fluorescence of a Single Dye Molecule Bound to Gold Nanoparticles. *J. Phys. Chem. B* **2006**, *110* (33), 16491–16498. https://doi.org/10.1021/jp0625816.

(25) Ben Haddada, M.; Blanchard, J.; Casale, S.; Krafft, J.-M.; Vallée, A.; Méthivier, C.; Boujday, S. Optimizing the Immobilization of Gold Nanoparticles on Functionalized Silicon Surfaces: Amine- vs Thiol-Terminated Silane. *Gold Bull.* **2013**, *46* (4), 335–341. https://doi.org/10.1007/s13404-013-0120-y.

(26) Abadi, S.; Navrazhnykh, L.; Greer, J. R. Functionalization of Shape Memory Polymers with Gold Nanoparticles. *SURF Final Rep.* **2019**.

(27) Baffou, G. *Thermoplasmonics: Heating Metal Nanoparticles Using Light*; Cambridge University Press, 2018.

(28) Jain, P. K.; Lee, K. S.; El-Sayed, I. H.; El-Sayed, M. A. Calculated Absorption and Scattering Properties of Gold Nanoparticles of Different Size, Shape, and Composition: Applications in Biological Imaging and Biomedicine. *J. Phys. Chem. B* **2006**, *110* (14), 7238–7248. https://doi.org/10.1021/jp057170o.

(29) Arbouet, A.; Christofilos, D.; Del Fatti, N.; Vallée, F.; Huntzinger, J. R.; Arnaud, L.; Billaud, P.; Broyer, M. Direct Measurement of the Single-Metal-Cluster Optical Absorption. *Phys. Rev. Lett.* **2004**, *93* (12), 127401. https://doi.org/10.1103/PhysRevLett.93.127401.

(30) Baffou, G.; Ureña, E. B.; Berto, P.; Monneret, S.; Quidant, R.; Rigneault, H. Deterministic Temperature Shaping Using Plasmonic Nanoparticle Assemblies. *Nanoscale* **2014**, *6* (15), 8984–8989. https://doi.org/10.1039/C4NR01644K.

(31) Jain, P. K. Taking the Heat Off of Plasmonic Chemistry. *J. Phys. Chem. C* **2019**, *123* (40), 24347–24351. https://doi.org/10.1021/acs.jpcc.9b08143.

VIII. Supplemental Information

Table S1. Summary of calculated fixed deformation and shape recovery values. Data shown are the means and standard deviations for FD and SR for five samples of each composition.

ID	*FD (7 days)*	σ_{FD}	*SR (40 °C)*	$\sigma_{SR\ (40\ °C)}$	*SR (55 °C)*	$\sigma_{SR\ (55\ °C)}$	*SR (70 °C)*	$\sigma_{SR\ (70\ °C)}$
A	97.40	0.86	2.49	1.14	26.48	4.20	75.03	10.76
B	92.06	1.47	3.75	1.25	44.78	6.24	92.54	4.43
C	69.56	2.81	12.39	2.73	82.47	3.16	98.35	0.63
D	59.45	5.36	21.38	4.12	81.88	1.95	93.69	1.04
E	96.83	1.22	1.65	0.40	10.37	2.13	61.05	8.80
F	94.13	1.20	2.14	0.61	19.45	6.25	59.02	5.23
G	79.72	1.85	9.17	3.27	46.93	3.56	100.1	1.28

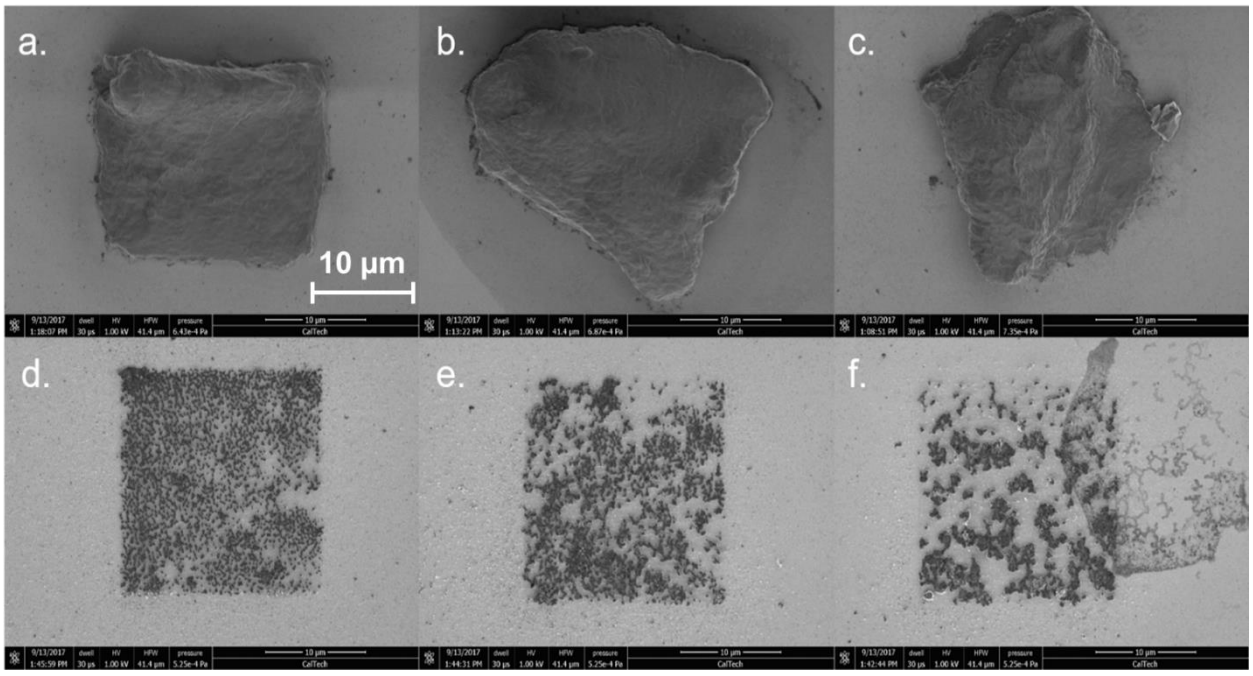

Figure S1. SEM images of DPEPA-containing microstructures written via TPL. Settings for laser power and scan speed respectively are (a) 20 mW and 100 µm s^{-1}; (b) 30 mW and 100 µm s^{-1}; (c) 40 mW and 100 µm s^{-1}; (d) 20 mW and 200 µm s^{-1}; (e) 30 mW and 200 µm s^{-1}; and (f) 40 mW and 200 µm s^{-1} ss.

Figure S2. MATLAB code used to smooth and correct the baseline of Raman data and perform peak analysis.

```
%% Variables
% all: set by user; dim x 2 matrix; column 1 wavenumbers,
column 2
% wavenumber: Raman shifts
% counts: counts/intensities associated with wavenumber
% baseline: baseline-corrected intensities
% baseline_sm: baseline-corrected intensities with
smoothing function applied
% pks: intensities of peaks
% locs: Raman shifts of peaks
% widths: full width at half max of peaks
% lowers: lower bound for trapezoid rule area calculation
% uppers: upper bound for trapezoid rule area calculation
% areas: areas under peaks

%% Set values for counts, & wavenumber
wavenumber = all(:, 1);
counts = all(:, 2);

%% Normalizing
% Performs baseline correction; adjust 'WindowSize' and
'StepSize' to improve fit
baseline = msbackadj(flip(wavenumber), flip(counts),
'WindowSize', 30, 'StepSize', 30);

baseline_sm = smooth(baseline);

% plots original, uncorrected data and baseline
% msbackadj(flip(wavenumber), flip(counts), 'WindowSize',
40, 'StepSize', 40)

% plot(flip(wavenumber), baseline_sm)

%% Peak finding
% Increase 'MinPeakProminence' to filter smaller peaks
[pks, locs, widths] = findpeaks(baseline_sm,
flip(wavenumber), 'MinPeakProminence', 80);

% plot
findpeaks(baseline_sm, flip(wavenumber),
'MinPeakProminence', 80)

%% Peak area calculation
```

```
lowers = locs - widths/2;
uppers = locs + widths/2;
areas = [];

% Area calculation via Trapezoid Rule
for i = 1:length(lowers)
    select = (wavenumber >= lowers(i))&(wavenumber <=
uppers(i));
    wavenumber_s = wavenumber(select);
    baseline_s = baseline_sm(flip(select));

    if length(wavenumber_s) > 1
        temp_area = trapz(flip(wavenumber_s), baseline_s);
        areas = [areas; temp_area];
    else
        areas = [areas; 0];
    end
end
```

Example of baseline correction for functionalized PETA.

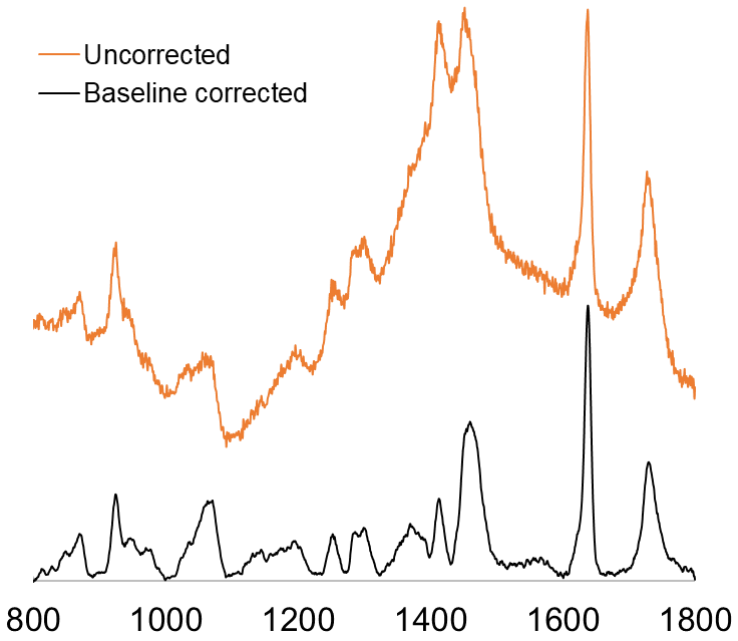

Table S2. Degree of polymerization data for pillars. All pillars shown were written using the sample laser power and scan speed.

Hatching distance(nm)	*Z-slice distance (nm)*	*DP % (C=C)*	$\sigma_{C=C}$	*DP % (C=O)*	$\sigma_{C=O}$
25	150	81.5	8.37	19.4	21.1
50	100	82.8	5.15	78.4	9.93
50	150	87.8	9.72	65.5	35.8
100	150	87.7	8.25	77.5	19.1

Figure S3. MATLAB code used for calculation of heat generated by LSPR, adapted from Baffou et al.[27]

```
%% Set variables
lambda0 = 532;           % wavelength in nm
a = 20;                  % radius in nm
n_s = (1 + 1.49)/2;      % average medium refractive index
n_Au = 0.5439+2.2343*1i;% gold refractive index at lambda0

m = n_Au / n_s;
k = 2*pi*n_s/lambda0;
x = k*a;
z = m*x;

%% Mie theory calculations
N = round(2+x+4*x^(1/3));
j = (1:N);
sqr = sqrt(pi*x/2);
sqrm = sqrt(pi*z/2);

phi = sqr.*besselj(j+0.5,x);
xi = sqr.*(besselj(j+0.5,x)+i*bessely(j+0.5,x));
phim=sqrm.*besselj(j+0.5,z);
phi1=[sin(x),phi(1:N-1)];
phi1m=[sin(z),phim(1:N-1)];
y=sqr*bessely(j+0.5,x);
y1=[-cos(x), y(1:N-1)];
phip=(phi1-j/x.*phi);
phimp=(phi1m-j/z.*phim);
xip=(phi1+i*y1)-j/x.*(phi+i*y);
```

```
aj=(m*phim.*phip-phi.*phimp)./(m*phim.*xip-xi.*phimp);
bj=(phim.*phip-m*phi.*phimp)./(phim.*xip-m*xi.*phimp);

% Efficiency calculation
Qsca=sum((2*j+1).*(abs(aj).*abs(aj)+abs(bj).*abs(bj)));
Qext=sum((2*j+1).*real(aj+bj));

% Cross section calculation
Cext=Qext*2*pi/(k*k);   % extinction cross sect. in nm^2
Csca=Qsca*2*pi/(k*k);   % scattering cross sect. in nm^2
Cabs=Cext-Csca;         % absorption cross sect. in nm^2

%% Change in temperature calculation
spot = pi*(10^5)^2;              % laser spot size (range:
10^5 - 10^7 nm)
I = 6/spot;                      % light irradiance (W/m^2)
k_m = (0.0262+0.19)/(2 * 10^9);  % average medium thermal
conductivity

% Calculate change in temperature of NP
deltaT = (Cabs * I)/(4 * pi * k_m * a);  % temperature
different from bulk
```